Theses and Dissertations   1. Thesis and Dissertation Collection, all items

2004-12

Design of two-axis capacitive accelerometer using MEMS

Lee, Chun Ming

Monterey California. Naval Postgraduate School

http://hdl.handle.net/10945/1226

NAVAL
POSTGRADUATE
SCHOOL

MONTEREY, CALIFORNIA

THESIS

DESIGN OF TWO-AXIS CAPACITIVE
ACCELEROMETER
USING MEMS

by

Lee, Chun Ming

December 2004

Thesis Advisor: Gamani Karunasiri
Second Reader: Jose Sinibaldi

THIS PAGE INTENTIONALLY LEFT BLANK

REPORT DOCUMENTATION PAGE		*Form Approved OMB No. 0704-0188*

1. AGENCY USE ONLY (*Leave blank*)	2. REPORT DATE December 2004	3. REPORT TYPE AND DATES COVERED Master's Thesis	
4. TITLE AND SUBTITLE: **Design of Two-axis Capacitive Accelerometer Using MEMS**		5. FUNDING NUMBERS	
6. AUTHOR(S) Lee, Chun Ming			
7. PERFORMING ORGANIZATION NAME(S) AND ADDRESS(ES) Naval Postgraduate School Monterey, CA 93943-5000		8. PERFORMING ORGANIZATION REPORT NUMBER	
9. SPONSORING /MONITORING AGENCY NAME(S) AND ADDRESS(ES) N/A		10. SPONSORING/MONITORING AGENCY REPORT NUMBER	
11. SUPPLEMENTARY NOTES The views expressed in this thesis are those of the author and do not reflect the official policy or position of the Department of Defense or the U.S. Government.			
12a. DISTRIBUTION / AVAILABILITY STATEMENT Approved for public release; distribution is unlimited.		12b. DISTRIBUTION CODE	

13. ABSTRACT (maximum 200 words)

MEMS technology is rapidly taking an important role in today's and future military systems. MEMS are able to lower the device size from millimeter to micrometer and maintain and sometimes surpass the performance of conventional devices. This thesis encompasses the knowledge acquired throughout the MEMS courses to design a two-axis capacitive accelerometer. The required acceleration and operating temperature range were $\pm50g$ in each axis and $-40°C$ to $+80 °C$, respectively. The accelerometer was also needed to survive within a dynamic shocking environment with accelerations of up to $225g$. The parameters of the accelerometer to achieve above specifications were calculated using lumped element approximation and the results were used for initial layout of it. A finite element analysis code (ANSYS) was used to perform simulations of the accelerometer under various operating conditions and to determine the optimum configuration. The simulated results were found to be within about 5% of the calculations indicating the validity of lumped element approach. The response of the designed accelerometer was 7 mV/g and with sensitivity of 1.3g at 3dB. It was also found that the accelerometer was stable in the desired range of operation including under the shock. Two axes sensing can be achieved using two identical accelerometers having their sensing axes perpendicular to each other.

14. SUBJECT TERMS MEMS, accelerometer			15. NUMBER OF PAGES 59
			16. PRICE CODE
17. SECURITY CLASSIFICATION OF REPORT Unclassified	18. SECURITY CLASSIFICATION OF THIS PAGE Unclassified	19. SECURITY CLASSIFICATION OF ABSTRACT Unclassified	20. LIMITATION OF ABSTRACT UL

NSN 7540-01-280-5500

Standard Form 298 (Rev. 2-89)
Prescribed by ANSI Std. 239-18

i

THIS PAGE INTENTIONALLY LEFT BLANK

DESIGN OF TWO-AXIS CAPACITIVE ACCELEROMETER USING MEMS

Lee, Chun Ming
Major, Taiwan Army
B.A., Chung Cheng Institute of Technology, 1990

Submitted in partial fulfillment of the
requirements for the degree of

MASTER OF SCIENCE IN APPLIED PHYSICS

from the

NAVAL POSTGRADUATE SCHOOL
December 2004

Author: Lee, Chun Ming

Approved by: Gamani Karunasiri
                     Thesis Advisor

                     Jose Sinibaldi
                     Second Reader

                     James Luscombe
                     Chairman, Department of Physics

THIS PAGE INTENTIONALLY LEFT BLANK

ABSTRACT

MEMS technology is rapidly taking an important role in today's and future military systems. MEMS are able to lower the device size from millimeter to micrometer and maintain and sometimes surpass the performance of conventional devices. This thesis encompasses the knowledge acquired throughout the MEMS courses to design a two-axis capacitive accelerometer. The required acceleration and operating temperature range were $\pm 50g$ in each axis and $-40^{\circ}C\ to +85^{\circ}C$, respectively. The accelerometer was also needed to survive within a dynamic shocking environment with accelerations of up to $225g$. The parameters of the accelerometer to achieve above specifications were calculated using lumped element approximation and the results were used for initial layout of it. A finite element analysis code (ANSYS) was used to perform simulations of the accelerometer under various operating conditions and to determine the optimum configuration. The simulated results were found to be within about 5% of the calculations indicating the validity of lumped element approach. The response of the designed accelerometer was 7 mV/g and with sensitivity of 1.3g at 3dB. It was also found that the accelerometer was stable in the desired range of operation including under the shock. Two axes sensing can be achieved using two identical accelerometers having their sensing axes perpendicular to each other.

THIS PAGE INTENTIONALLY LEFT BLANK

TABLE OF CONTENTS

THIS PAGE INTENTIONALLY LEFT BLANK

LIST OF FIGURES

THIS PAGE INTENTIONALLY LEFT BLANK

LIST OF TABLES

THIS PAGE INTENTIONALLY LEFT BLANK

ACKNOWLEDGMENTS

First, I would like to express my deep appreciation to the staff and faculty of Naval Postgraduate School who supported and assisted me in finishing the courses I took during the past two years. They all have made my life more vivid and colorful than before.

Second, I would like to thank my thesis advisors, Professor Gamani Karunasiri and Professor Jose Sinibaldi. They always did their best to explain the theory on MEMS to me whenever I felt confused. They also helped me learn all the software required to design MEMS devices. I will not forget their patient instruction and guidance.

Next, I want to thank my dear friend, Dr. Byungki Kim. I owe him much for his kindness to instruct me step by step on how to use the macro command language for ANSYS. He contributed a lot of his personal time to work with me, which help me complete my thesis.

Finally this thesis is dedicated to my wife and children. I thank them from the bottom of my heart for all of their support and specially for their encouragement to continue my academic studies at NPS.

Lastly, I would like to finish these acknowledgements by saying that these past two years will always be some of the most beautiful memories of our lives!

THIS PAGE INTENTIONALLY LEFT BLANK

I.   INTRODUCTION

A.   BACKGROUND

The use of microelectronic processing techniques to fabricate miniature mechanical devices has attracted considerable attention during the last decade [1]. These devices are generally known as micro electro mechanical systems or MEMS [2][3]. The current MEMS technology allows integration of mechanical, optical, fluidic, and electrical components [4]. Because of the advantage of size ranging from millimeter to micrometer, MEMS devices broaden their applications to many fields from commercial to medical and military products. There are many successful commercial MEMS products available in the market, such as inertial guide system, accelerometer, pressure and chemical sensors, micro-optics and micro fluidic pumps [5].

Accelerometers are part of the most successful MEMS products available since 1980's.The basic mechanism of sensing the acceleration is to monitor the displacement of a proof mass attached to a spring as schematically illustrated in Figure 1.
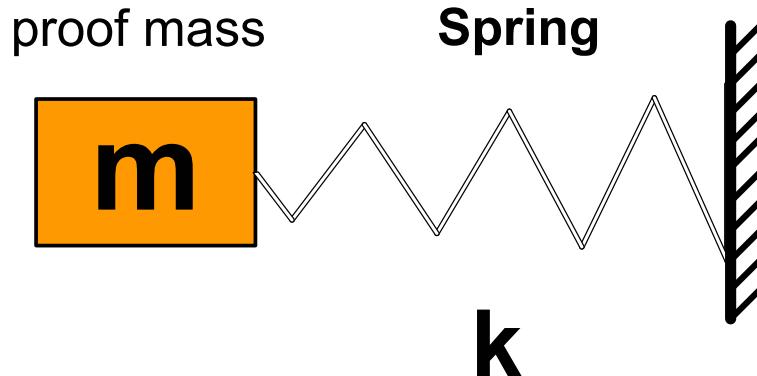
Figure 1.   Basic accelerometer operation mechanism.

If the displacement of the proof mass is δx for a given acceleration (a), the relationship between a and dx can be written as Equation (1)[6],

$$ma = k\delta x \Rightarrow \delta x = \frac{a}{\omega_o^2} \qquad\qquad (1)$$

where k is the spring constant and ω_o is the resonant frequency of the system. It can be seen from Equation (1) that for higher sensitivity it is necessary to have a lower resonant frequency or a softer spring for a given mass. However, such a system would have a slower response time and sudden changes of acceleration may not be measured accurately [6]. Note that the above quasi-static derivation is true only for acceleration changes are slower than the resonant frequency [6]. For applications involving rapid changes of acceleration, a higher resonant frequency is needed which can lower the resolution as expected from Equation (1). There are several approaches of sensing the amount of displacement of the proof mass that include as piezoresistive [7], capacitive [8][9], tunneling [10] [11] and optical [12][13] changes. The capacitive accelerometers play an important role due to their good temperature stability, high sensitivity and low power consumption [14]. In the following, a brief description of different acceleration sensing mechanisms employed to date will be presented.

1. Capacitive Accelerometer

In a capacitive accelerometer, the displacement of the proof mass is monitored by changes in capacitance of a parallel plate capacitor where one of the plates is attached to a spring as schematically illustrated in Figure 2. When the external acceleration is applied to the accelerometer, the moving plate (proof mass) will move from its rest position that changes the capacitance between the moveable and fixed plates. The change in capacitance is usually measured using bridge circuit and will be discussed in detail later.
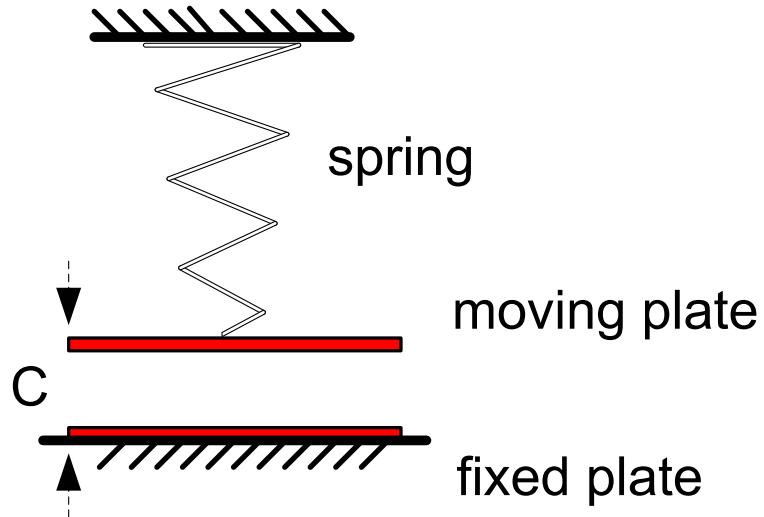
Figure 2.   Capacitive accelerometer operation.

2.   Tunneling Accelerometer

Tunneling accelerometer utilizes the tunneling current between a tunneling tip attached to the proof mass and counter-electrode to sense the displacement as shown in Figure 3.
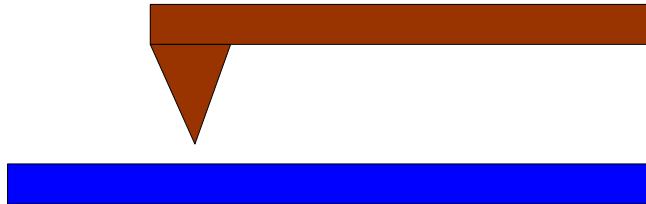
Figure 3.   Basic tunneling accelerometer operation mechanism.

The operation tunneling accelerometer requires the tip and the counter-electrode separation within a few angstroms. During the operation a constant tunneling current is maintained between the tip and electrode using an external circuit. Under acceleration the separation between the tip and electrode changes which in turn affects the tunneling current and the circuit will respond to the current change and adjust the voltage to restore

3

the tunneling current. The amount of voltage needed can be correlated with the acceleration [10]. This type of accelerometer yields very high sensitivity due to the fact that the tunneling current is very sensitive to the displacement [11]. The drawbacks of this design are large noise levels at low frequencies as well as requirement for a high voltage power supply for maintaining tunneling current. Lately there have been some efforts to develop a low-voltage version of the tunneling accelerometer with the hope of mitigating some of the aforementioned problems [15].

3.   Piezoresistive Accelerometer

The piezoresistive accelerometer is based on strain gauge technology and is best suited for low frequency applications [7]. It was the first micromachined accelerometer produced and one of the first to be commercialized [7]. The operation principle is based on the change of resistance due to stress generated by deflection of Si beams attached to the proof mass as illustrated in Figure 4. By positioning the silicon piezoresistors at the highest stress point (usually where the beam attaches the substrate) the resistance change can be maximized. Subsequently, a resistive half-bridge or full bridge can be formed by employing two or four piezoresistors to measure the resistance change [7].
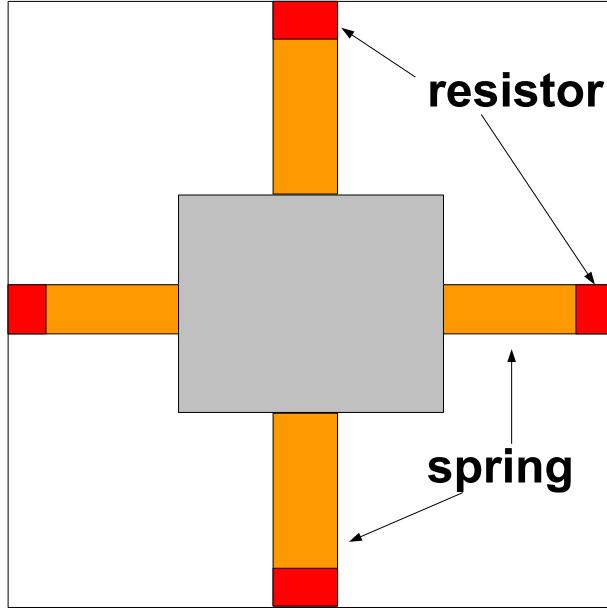
Figure 4.   Schematic diagram of a piezoresistive accelerometer.

4

The main advantages of piezoresistive accelerometers are their simple structure and fabrication processes. However, comparing to capacitive accelerometers, the larger temperature sensitivity and smaller overall sensitivity are its drawbacks [16].

4.   Thermal Accelerometer

Thermal accelerometers take advantage of heat transfer characteristics between two plates of which one acts as a heater and the other as the heat sink [13]. The heat flow rate is inversely proportional to their separation distance [13]. If one plate can move relative to the other during the acceleration, the heat flow will change which affects the temperature of the heat sink. This temperature can be measured using thermopiles which can be correlated to the amount of acceleration. Another type of thermal accelerometer that does not have any moving mechanical parts, it instead uses free-convection heat transfer of a small hot air bubble in a seal chamber as its fundamental working function [13]. Thermally isolated heaters in this device form a hot air bubble. Because of the acceleration, the heat distribution of the bubble will be changed and becomes asymmetric with respect to the heater. By utilizing two symmetrically placed temperature sensors, the heat profile and acceleration can be measured. The initial prototype's sensitivity can approach 0.6 mg, but has a theoretical limit of sub-µg sensitivity [13].

THIS PAGE INTENTIONALLY LEFT BLANK

II.   REQUIREMENTS AND EVALUATION

A.   REQUIREMENTS

This work involved the design of a two-axis (x, y) accelerometer, which can sense the acceleration on a plane with specific parameters. The accelerometer should have the ability to measure the acceleration of ± 50g while able to maintain a 20 kHz frequency response for each axis. The accelerometer should also survive a maximum shock of ± 225g in any direction. The design's layout should fit within an area of 1 cm^2. The operating temperature for the accelerometer was -40°C to +85°C, but should be able to survive in temperatures from -45°C to +125°C. To reduce operational costs, a self-test function should be designed in place and not required an operator. All of these requirements make up the limitations of the accelerometer designed in this thesis. Table 1 summarized these requirements.

Table 1.   Requirements for capacitive accelerometer design.

	Requirements of Design			
Axis	Acceleration	Surviving shock	Surviving Temperature	Operating Temperature
X	± 50g	± 225g	-45°C to +125°C	-40°C to +85°C
Y	± 50g	± 225g	-45°Cto+ 125°C	-40°C to +85°C

B.   DESIGN TOOLS

The entire design was carried out using MEMS Pro software available to us and the fabrication to be compatible with the PolyMUMPs process available via MEMSCAP [17]. It included L-edit, S-edit, T-spice and ANSYS for layout and various simulations. Each tool has its unique function. The MEMS library came with the design software

provided a number of components and schematics to assemble and to conduct simulations. The following were the main tools used to perform the work in this thesis.

1.   L-Edit

L-Edit was a graphical layout editor for MEMS devices. The use of different colors, predefined in the system, represented different layers, which correlate to the various microfabrication processes. The design process was drastically simplified, to the point that it appeared, at times, that we were simply drawing a picture. In addition to the fundamental components such as: box, polygon, circle, line and wire; the library also provided complex models, such as: suspension elements and electro-mechanical transducers. The powerful 3-D model simulation function clearly constructed the device step by step as if undergoing the actual microfabrication processes; this made very easy to identify design flaws in the early stages.

2.   ANSYS

ANSYS was a finite element analysis software capable of performing multi-physics simulations. In other words, ANSYS provided the ability of performing structural, thermal, electrostatic, electromagnetic, and fluidic analysis all at once. Using the graphical user interface in conjunction with an ANSYS scripting language, we could program customized functions to build the computer models and/or transfer the CAD models, into the simulation environment, properly mesh the MEMS devices, assigned boundary conditions, solved the problems and viewed the results. [18]. Therefore, it was possible to quickly change the model's dimensions, material properties, displacements and stresses.

C.   EVALUATION

The literature search on different accelerometer designs revealed that all the approaches have their unique characteristics with both advantages and shortcomings. The simplicity of design and high reliability when compared to other designs prompted us to use differential capacitive accelerometer concept over others [8].

The fundamental operating principle for capacitive accelerometer was as follows: a moveable proof mass connected between two fixed springs (see Figure 5) would be activated when an acceleration was applied to create a force. Hence, under this acceleration, the gap between the two different voltage electrodes would change and create a differential capacitor. Thus the change in capacitance could be measured which can be translated to the amount of acceleration. This was the most popular approach and has been adopted working function used in all of the commercial airbag sensors due to its ruggedness and high sensitivity [14]. The design presented in this thesis geared towards the use of a multi-user microfabrication facility/process known as PolyMUMPS. The decision to design the accelerometer with this predefined process in mind was tied down to the low costs involved when using such multi-user facilities and also due to the very high reliability of this microfabrication process, which has turned out over 69 different fabrication runs with outstanding success [19].
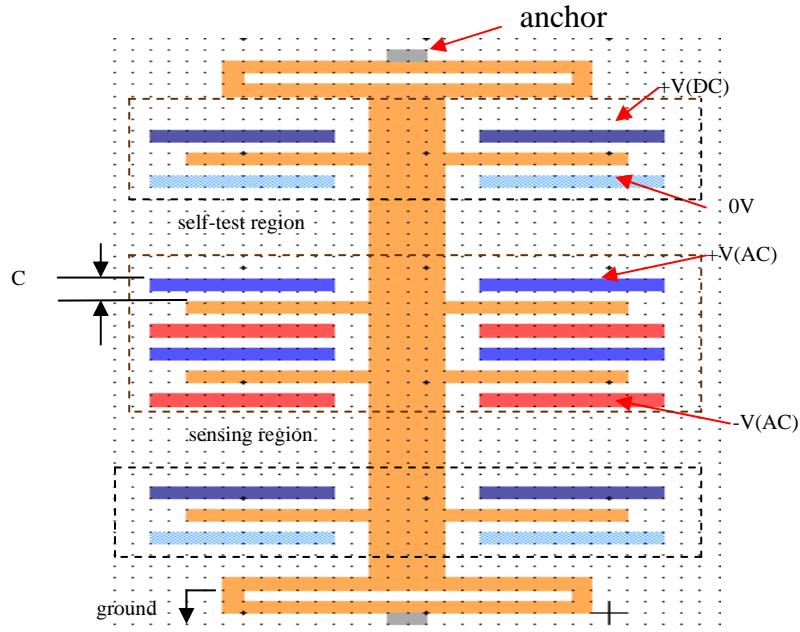

Figure 5.   Schematic of Accelerometer.

The PolyMUMPS process, started in 1992, was a surface micromachining process containing a series of coating and etching procedures [17]. It contained three-layers of doped polysilicon, which worked as both structural and conducting layers. The

9

polysilicon layers were separated by silicon dioxide layers that acted as sacrificial layers. In addition there was a silicon nitride layer at the bottom for isolation and metal on the top for making electrical contacts. This was the most popular process that can be used for fabricating variety of MEMS designs. Other more complex processes involving up-to 5 structural layers were available (such as the Summit IV process from SANDIA National labs,) but the extra layers were deemed not necessary for our accelerometer design. The three structural layers were sufficient for to the current design of the two-axis accelerometer and preliminary calculations indicate that 3 layers were also sufficient for extending the design to 3-axes.

Since both the x and the y-axis laid on the same plane it made sense to create identical accelerometers for both axes but position them orthogonal to each other. In addition to simplifying the accelerometer design and device layout, it also effectively reduced the possible errors during the design. In order to maximize the sensing area of the device, the x and y-axis accelerometer were designed to be long and contained a large number of differential capacitor units. Before drawing the accelerometer in L-Edit, hand calculations and spreadsheet computations in EXCEL played a major role in this work. Subsequent finite element simulations in ANSYS were performed to verify the results and to come-up with an optimized design.

It was a common practice to include a test section where an internal force can be applied for self-testing of the performance. This can be achieved by using a capacitor with a moving plate as illustrated in Figure 2.

The accelerometer was composed of a center plate (proof mass) that was suspended between a pair of springs. Comb fingers (called electrodes) attached to the two sides of the plate created a differential capacitor by interacting with the outside fixed electrodes as shown in Figure 5. The moveable and fixed electrodes were the two fundamental components of differential capacitor sensor. The former electrodes attached to the central plate were responsible for sensing acceleration. The latter ones were the voltage suppliers. Movement of the electrodes changed the differential capacitance, which was measured by the chip circuitry.

III. DESIGN METHODOLOGY

In the previous chapter, we have described the operational principle of capacitive accelerometers and various components necessary for sensing the acceleration as well as self-testing. This chapter presented the analysis of the design of various components to satisfy the design requirements.

A.   SPRING

Under acceleration, the proof mass of the accelerometer experienced a force. The displacement of the proof mass will compress one spring and stretch the other until the force due to acceleration cancelled by the spring forces. Thus, the combined spring constant of the springs will determine the amount of proof mass displacement and hence the signal generated by the sensing capacitors. Therefore, how to choose a suitable spring became a key piece of this work. In MEMS the most convenient way to make a spring was to use a folded structure as shown in Figure 6.
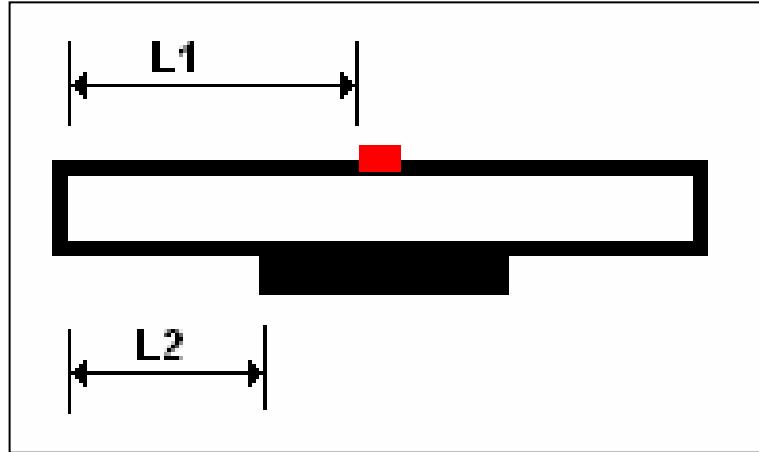

Figure 6.   Schematic diagram of a folded spring made of polysilicon [From: Ref. 20].

The spring was composed of four beams made of polysilicon layers. The red square area in Figure 6 was the anchor, fixing the spring on to the substrate. The central plate (proof mass) was connected from the bottom black area to the other symmetrical

11

spring. The spring constant (K) determined the extent of displacement of the proof mass and could be calculated by the formula in Equation (2) [21]

$$K = (\frac{\pi^4}{6})[\frac{EWH^3}{(2L_1)^3 + (2L_2)^3}] \qquad (2)$$

Where E was the Young's modulus of plysilicon, W was the beam width, H was the beam thickness and L1, L2 were the beam lengths as shown in Figure 6.

From the above formula it can be seen that the spring constant was controlled by the lengths (L_1 and L_2) if the H and W were fixed. Other important parameter in the design of an accelerometer was the proof mass (m) since the spring constant and proof mass determined the resonant frequency (ω_0) as given in Equation (3):

$$\omega_0 = 2\pi f = \sqrt{\frac{K}{m}} \rightarrow m = \frac{K}{\omega_0^2} \qquad (3)$$

The resonant frequency determined how fast the accelerometer can responds to a changing acceleration or the bandwidth of operation. Our design required the bandwidth to be 20 kHz and it was necessary to set the resonant frequency to be higher than the bandwidth to avoid unstable operation [22]. In the present design, the resonant frequency was set to be about five times the bandwidth or 100 kHz. For simplicity, lengths L_1 and L_2 assumed to be the same and the dimensions of W and H were also taken to be the same as the polysilicon layer thickness (2 μm). In order to estimate the proof mass and that gives resonant frequency of about 100 kHz, we have first calculated the total spring constant due to the two springs (2K) using Equation (3) and the results were shown in upper section of Table 2. Next, we have calculated the resonant frequency using the calculated spring constants and varying the proof mass and the results were shown in the lower section of Table 2.

Table 2. Calculation of spring constant for different combination of length, spring constant and mass.

L_1 (μm)	35	60	70	80	90	100
L_2 (μm)	35	60	70	80	90	100
2*k (N/m)	1.14E+02	2.25E+01	1.42E+01	9.51E+00	6.68E+00	2.44E+00
m	f_n	f_n	f_n	f_n	f_n	f_n
(kg)	(kHz)	(kHz)	(kHz)	(kHz)	(kHz)	(kHz)
1.76E-10	127.8633	56.9668	45.2066	37.0010	31.0088	18.7212
1.86E-10	124.3786	55.4143	43.9745	35.9926	30.1637	18.2110
1.96E-10	121.1641	53.9821	42.8381	35.0624	29.3841	17.7403
2.06E-10	118.1867	52.6556	41.7854	34.2008	28.6621	17.3044
2.16E-10	115.4184	51.4223	40.8067	33.3997	27.9907	16.8991
2.26E-10	112.8360	50.2717	39.8936	32.6524	27.3645	16.5210
2.36E-10	110.4196	49.1951	39.0393	31.9532	26.7784	16.1672
2.46E-10	108.1520	48.1848	38.2376	31.2970	26.2285	15.8352
2.56E-10	106.0186	47.2344	37.4833	30.6796	25.7111	15.5228
2.66E-10	104.0067	46.3380	36.7720	30.0974	25.2232	15.2282
2.76E-10	102.1051	45.4908	36.0997	29.5471	24.7620	14.9498
2.81E-10	101.193	45.0842	35.7771	29.2831	24.5408	14.8162
2.86E-10	100.3042	44.6884	35.4629	29.0260	24.3253	14.6861

The analysis showed that in order to achieve 100 kHz resonant frequency, it necessary to have $L_1 = L_2 = 35$ μm and proof mass of 2.81×10^{-10} Kg (less than 0.3 ng).

B. PROOF MASS AND ELECTRODES

The proof mass included the masses of the central plate and all the moving electrodes as illustrated in Figure 7. In order to perform the self-test function, the whole structure was separated into two parts, the sensing region and the self-test region.
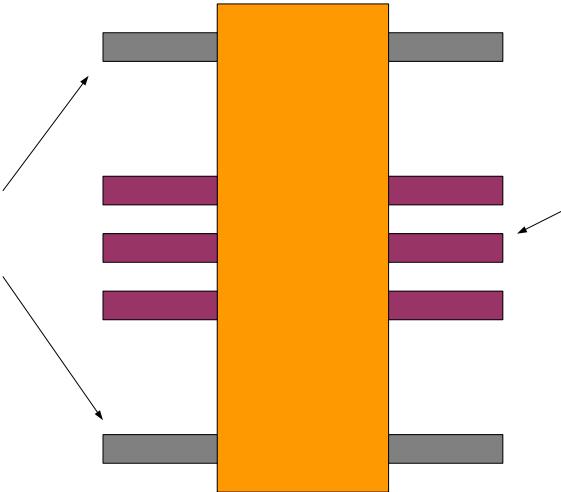
Figure 7.   Schematic diagram of proof mass with sensing and self-test electrodes.

1.   Sensing Region

Sensing region was responsible for detecting motion when the acceleration was applied. According to Table 2, the proof mass including the central plate and all of the connected electrodes should be limited to about 2.81×10^{-10} Kg. The attached finger-like polysilicon structure in the central plate was the sensing element. .

The moving and fixed fingers formed a parallel plate capacitor and the capacitance can be estimated using Equation (4).

$$C = \frac{\varepsilon_0 A}{g_{ap}} \tag{4}$$

Where ε_0 was the permittivity, A was the total overlap area between all the fingers in the sensing region and g_{ap} was the separation between adjacent fingers. Since the changing capacitance was proportional to the area (A), for achieving higher signal it was necessary to increase the area or number of fingers. By setting the value of the capacitance to be about 100 fF, the number of fingers required was found to be about 112. The parameters used in this estimation were summarized in Table 3. These electrodes can be placed on either side of the proof mass as illustrated in Figure 7.

14

Table 3.   Parameters of electrodes attached to central plate.

	Sensing Electrodes Design Data
Total Length (μm)	120
Overlap Length (μm)	100
Width (μm)	2
Depth (μm)	2
Gap between fingers (μm)	2
ε_0 (F/m)	8.854×10^{-12}
Density of Polysilicon (Kg/m^3)	2330

The readout of the capacitance change was typically achieved by applying an AC voltage to the sensor capacitor. The frequency of the AC voltage was chosen to be away from the resonant frequency of the accelerometer (usually higher to reduce 1/f noise) to minimize the displacement of the fingers by electrostatics forces within the sensor capacitor.

2.   Self-Test Region

In this region, the design considerations were the same as that in the sensing region except for the applied voltages and number of electrodes. Initially, 20% of the sensing electrodes (24) were selected for generating an internal electrostatic force for self-testing. These were located on both sides of the central plate and were separated into 4 regions as shown in Figure 5. Each region was made of 6 electrodes and the dimensions were all the same as those found in Table 3.

3. Proof Mass

To achieve the required total mass, the dimensions of the central plate was determined by subtracting the mass of all the fingers (including the ones used for testing) and found to be 812 µm for length and 34 µm for width. The calculation of mass of the central plate and 136 electrodes was shown as below.

$$m_{central} = \rho V = 812um \times 34um \times 2um \times 2330Kg/m^3 = 1.29 \times 10^{-10} Kg$$

$$m_{112\,fingers} = 136 \times 2um \times 2um \times 120um \times 2330Kg/m^3 = 1.52 \times 10^{-10} Kg$$

$$M_{proof} = m_{central} + m_{136\,fingers} = 2.31 \times 10^{-10} Kg$$

Force on the proof mass was achieved by applying a DC voltage to the self-test capacitor. The amount of force as a function of DC voltage can be estimated using the stores energy (W) on the capacitor as followed:

$$W = \frac{1}{2}CV^2 \tag{5}$$

Using Equation (5) the electrostatic force F can be found as

$$F = -\nabla W = -\frac{\partial W}{\partial g_{ap}} = \frac{\varepsilon_0 A V^2}{2g_{ap}^2} \tag{6}$$

If one plate was free and the other one was fixed in the parallel capacitor, it would mean that the free plate could be driven by electrostatic force. And the force controlled by voltage was inversely proportional to g_{ap}^2 and directly proportional to V^2. The force between each pair of movable and fixed electrodes was given by

$$F = \frac{\varepsilon_0 A V^2}{2g_{ap}^2} = \frac{(8.854 \times 10^{-12} F/m) \times (100\mu m \times 2\mu m) \times (15)^2}{2 \times (2\mu m)^2}$$

.

$$= 4.98 \times 10^{-8} Nt$$

Combining Hook's Law and Newton's Second Law (Equation (7) as well as the effective spring constant, one could compute the displacement of the proof mass under the conditions of self-test, and under 50g and 225g of acceleration.

$$F = kx = Ma \tag{7}$$

Using the total mass of the proof mass of 2.81×10^{-10} Kg, the deflections under 50g and 225g were found to be 1.20×10^{-9} m and 6.01×10^{-9} m, respectively. The corresponding voltages required for achieving above displacements using the self-test capacitor can be estimated using Equation (6) and found to be about 5 V and 11 V, respectively.

At this point, all of the preliminary design parameters as well as operating consideration have been completed. The estimated design parameters of the accelerometer were used to lay out the design using L-Edit in MEMSPro software as shown in Figure 8. In addition to layout, L-edit also provided the parameters needed for finite element modeling using ANSYS software. ANSYS was then used to run 3-D simulations that took into account all nonlinearities in our design and the results were used to optimize and perform a system analysis of this accelerometer design. The 2-D and 3-D views of the various components of the accelerometer were shown in Figure 9 to Figure 12.

Self-Test Region
(24 electrodes)

Overlap length: 100 μm
Gap: 2 μm

+15V AC

-15V AC

Sensing Region
(112 electrodes)

0V DC

+5V DC
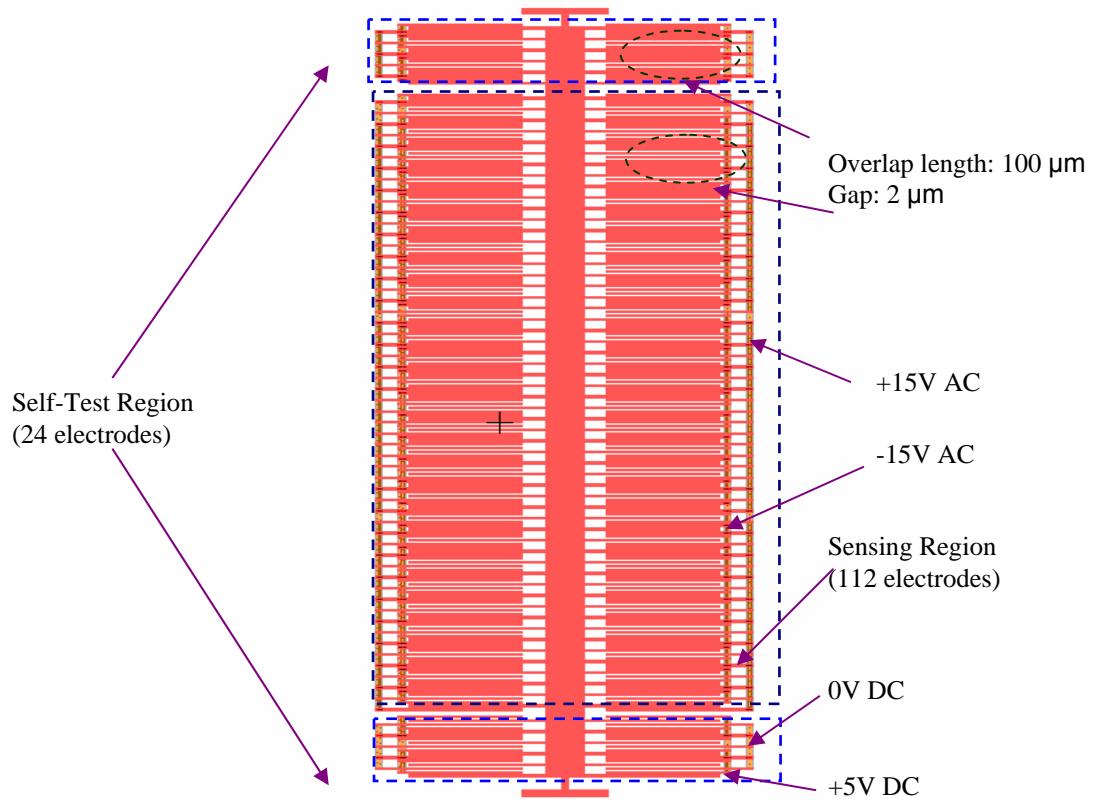
Figure 8.   Schematic of accelerometer in L-edit.
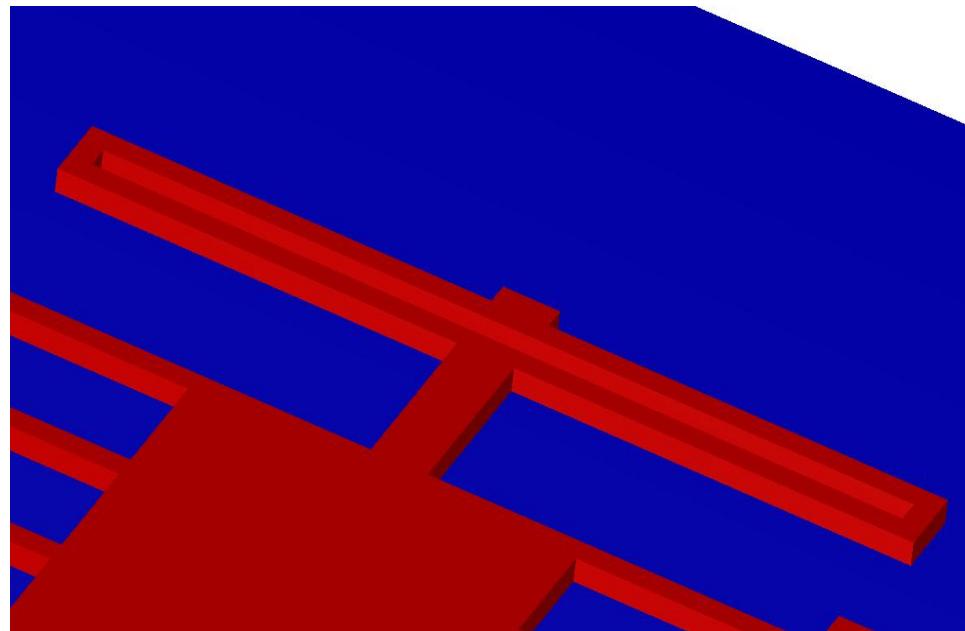

Figure 9.   3-D highlight view of folded spring.
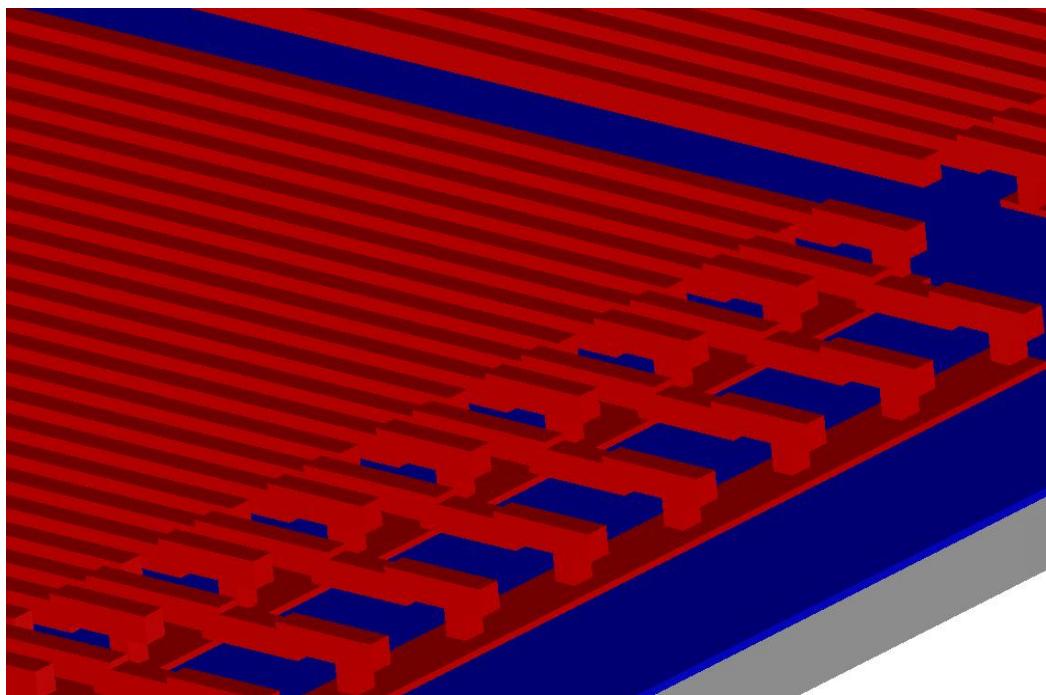
Figure 10.   3-D highlight view of fixed electrodes.
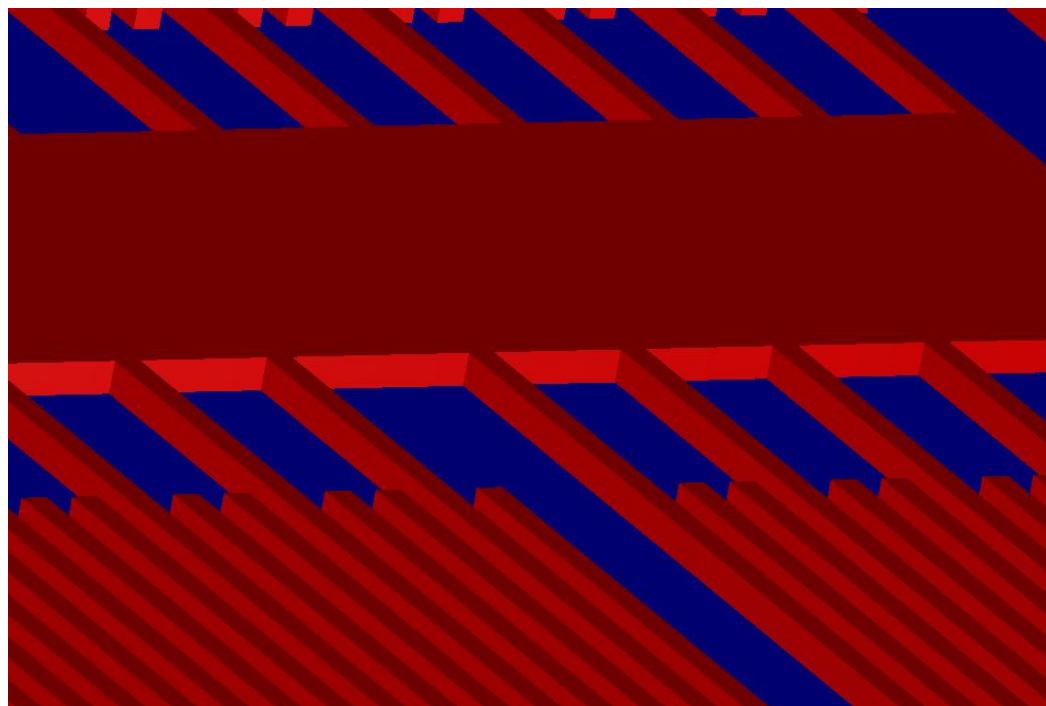
Figure 11.   3-D highlight view of moveable electrodes attached to central plate.
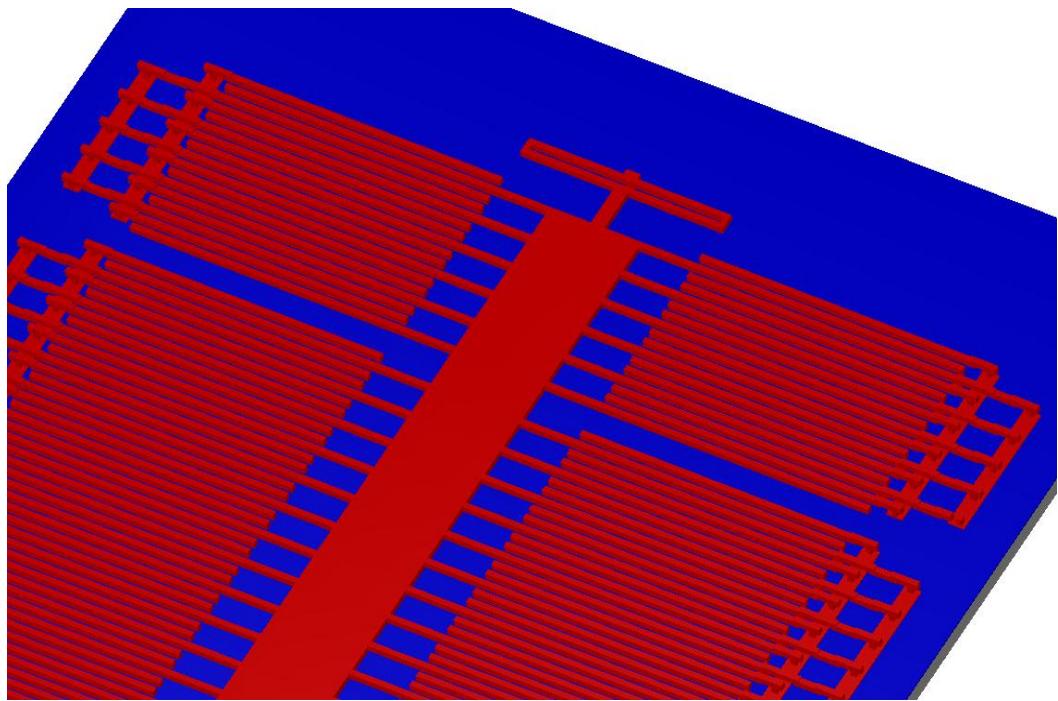
Figure 12.   Highlight view of self-test and sensing region.

IV.   SIMULATION AND COMPARISON

A.   PROCESS

In order to perform a realistic simulation of the performance of the accelerometer, it was required to export the 3-D model file including boundary conditions from L-edit into ANSYS. Second, the ANSYS would perform the simulation depending on the various forces applied by the user. Since the proof mass activated the movement due to acceleration, the supplied force was also put on the central plate body and denoted as a force point in ANSYS. The simulated results would show displacements and stresses in each axis. However, the axial direction of the applied force should have a much larger displacement than the other two axes. The off-axis effects were important for the stability analysis, which will be discussed in detail later. According to the requirements described in Section I, the device should survive 225g of acceleration – note that measurements at these high acceleration levels were not required, but it should survive such shocks. The easiest way to make sure that it worked was to check whether the structure exceeded its stress limits under 225g.

B.   RESULTS

1.   50g Force

The Figures 13-17 showed the ANSYS simulation of the designed accelerometer under a 50g force applied on the proof mass. In Figures 13-17, the amount of deflection was color corded with red being the highest deflection. The maximum deflection was found to be about 1.06×10^{-9} m. If we highlighted the local area of the springs, it can be easily seen that the deflection was minimum near the anchors and increased gradually towards the center of the spring where the proof mass was connected. All of these results showed similar trends as the preliminary calculations presented in the previous chapter. Comparing to the deflection along the force direction (y-axis), the deflection of x-axis and z-axis were very small, 2% and 0.2% respectively. The difference between the preliminary calculations and the ANSYS full simulations was less than 5%. The calculated and ANSYS simulated deflections for 50g force were summarized in Table 4.

$$difference\% = \frac{1.21 \times 10^{-9} - 1.16 \times 10^{-9}}{1.16 \times 10^{-9}} = 4.3\%$$

Table 4.   Displacement of three axes under 50g force.

Item		Condition	Result	
		Applied	Calculation	Simulation
Acceleration		50 g		
Force		1.37×10^{-7} Nt		
Deflection	ux			2.53×10^{-11} m
	uy		1.21×10^{-9} m	1.16×10^{-9} m
	uz			2.40×10^{-12} m
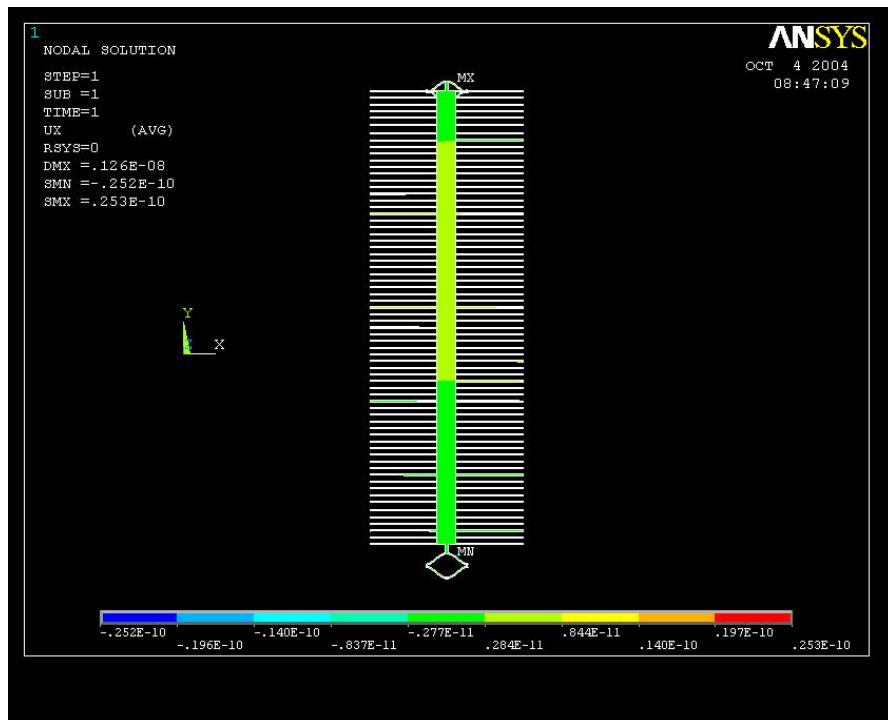
Figure 13.   Displacement along x-direction for 50g force using ANSYS.
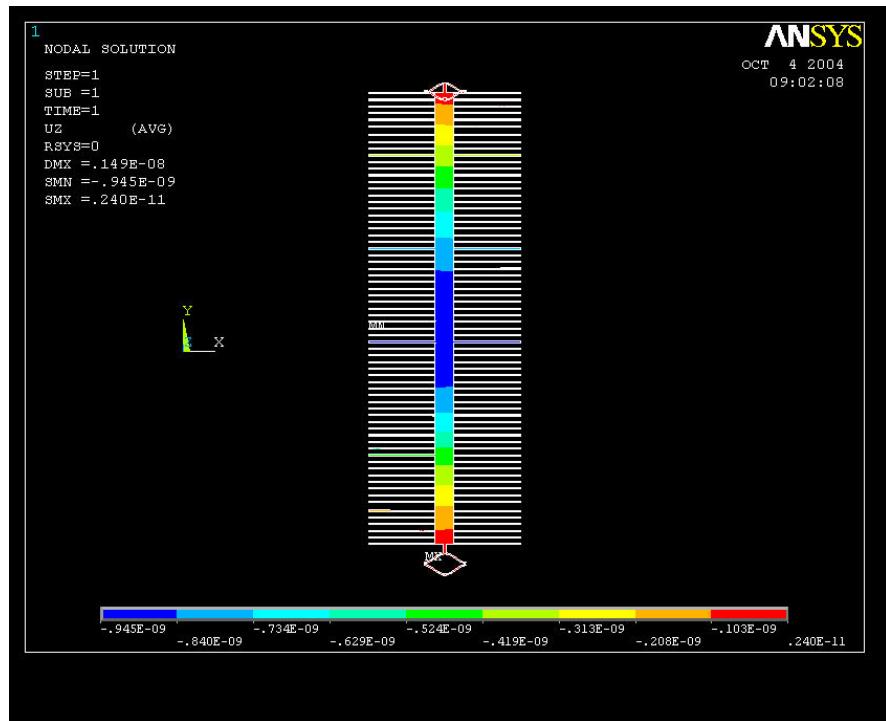
Figure 14.   Displacement along z-direction for 50g force using ANSYS.
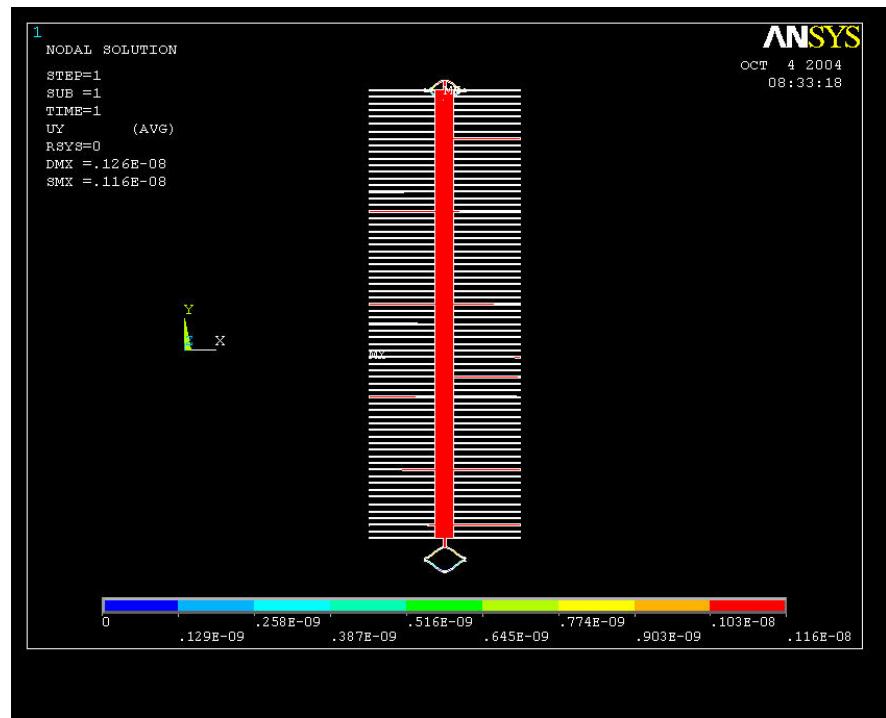

Figure 15.   Displacement along y-direction for 50g force using ANSYS.
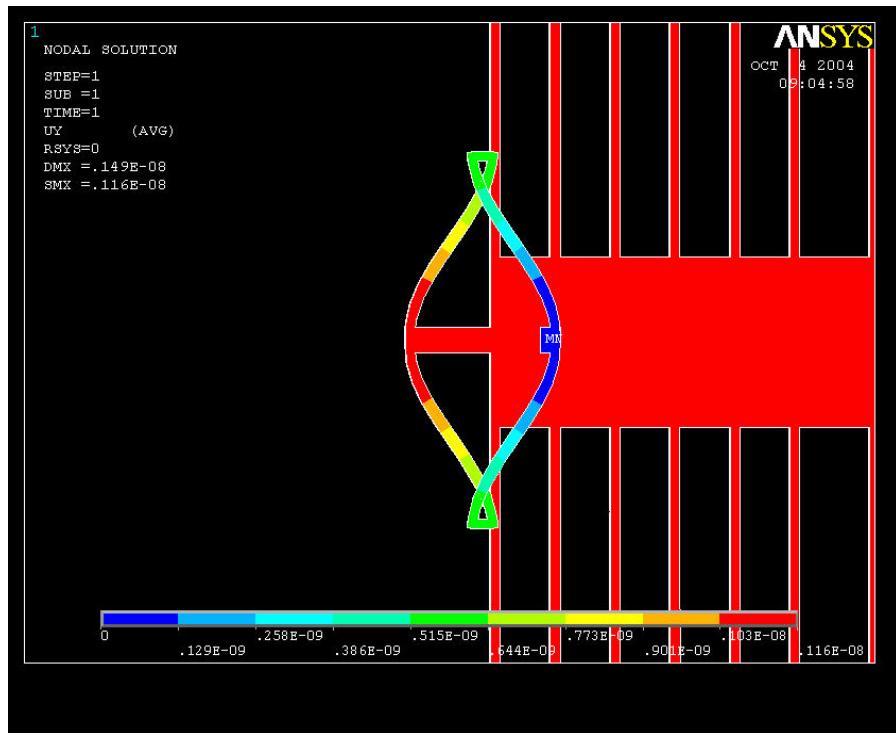
Figure 16.   Expanded view of the spring compression along y-direction under 50g force.
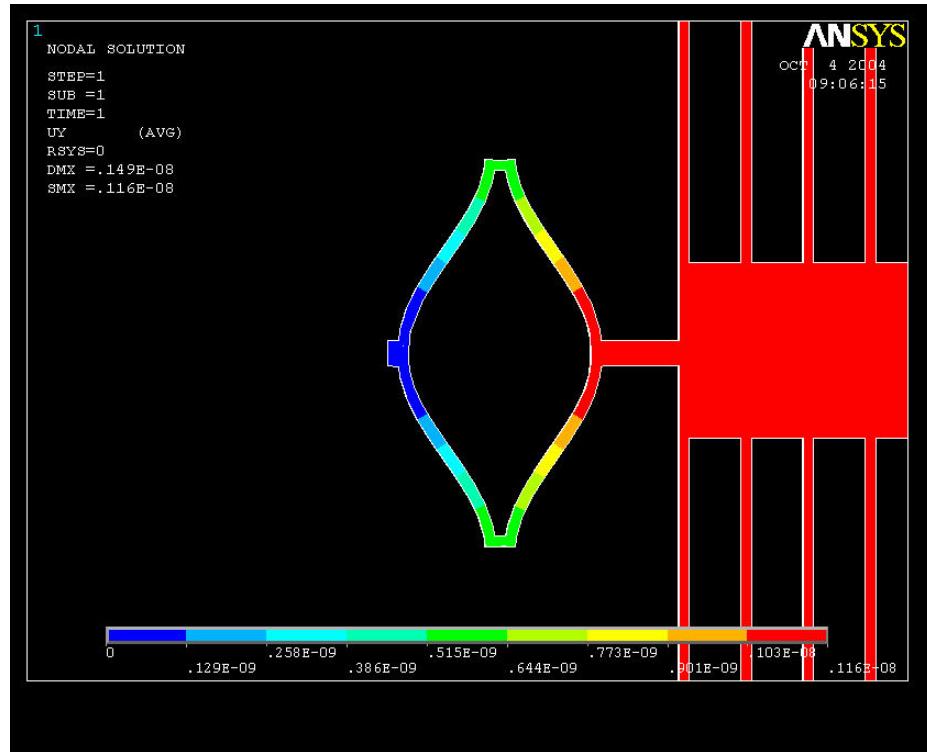

Figure 17.   Expanded view of the spring expansion along y-direction under 50g force

2. 225g Force

Similarly to the 50g simulation, one could put the force of 225g on the central plate. In this simulation, it was necessary to pay attention to stresses in the beams of the springs in addition to displacements. Because the connecting region of springs to proof mass displayed the maximum displacement, the ANSYS simulations were carried out highlighting these sections as shown in Figures 18-19. The simulated results yielded displacement of about $5.79 \times 10^{-9} m$ along the direction of the force (y direction). This was about a factor of 5 larger than the displacement under 50g force. The calculated value was higher than the simulation by almost 4%. The Table 5 summarized the calculated and simulated displacements.

$$difference\% = \frac{6.01 \times 10^{-9} - 5.79 \times 10^{-9}}{5.79 \times 10^{-9}} = 3.8\%$$

Table 5.   Displacement of three axes under 225g force.

Item		Condition	Result	
		Applied	Estimation	Simulation
Acceleration		225 g		
Force		6.85×10⁻⁷ Nt		
Deflection	Ux			1.25×10^{-10} m
	Uy		6.01×10^{-9} m	5.79×10^{-9} m
	Uz			1.08×10^{-11} m
Stress	Y		Specification 130 Mpa	2.30Mpa

For the other two axes (x and z) yielded displacements of about $1.25 \times 10^{-10} m$ and $1.08 \times 10^{-11} m$, respectively. The ratio of displacement comparing to y-axis was the same as obtained for 50g force, 2% and 0.2% respectively. Meanwhile, the maximum stress in the anchor using the data in Figures 20-21 was about 2.3 MPa. It was still smaller than

material elastic limit of 130 MPa. This suggested that the springs can withstand forces larger than 225g.
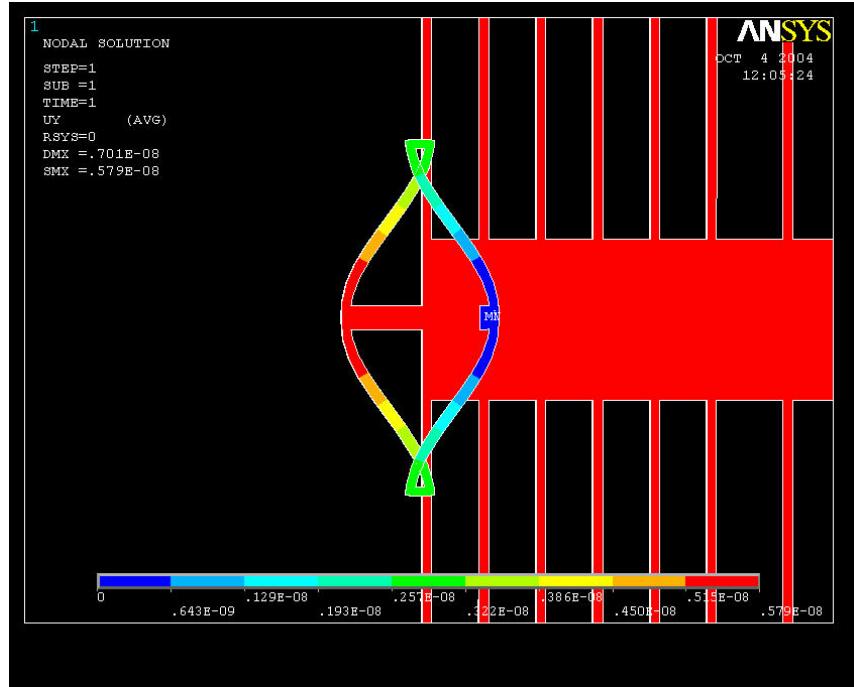
Figure 18.   Expanded y-displacement for compression side under 225g.
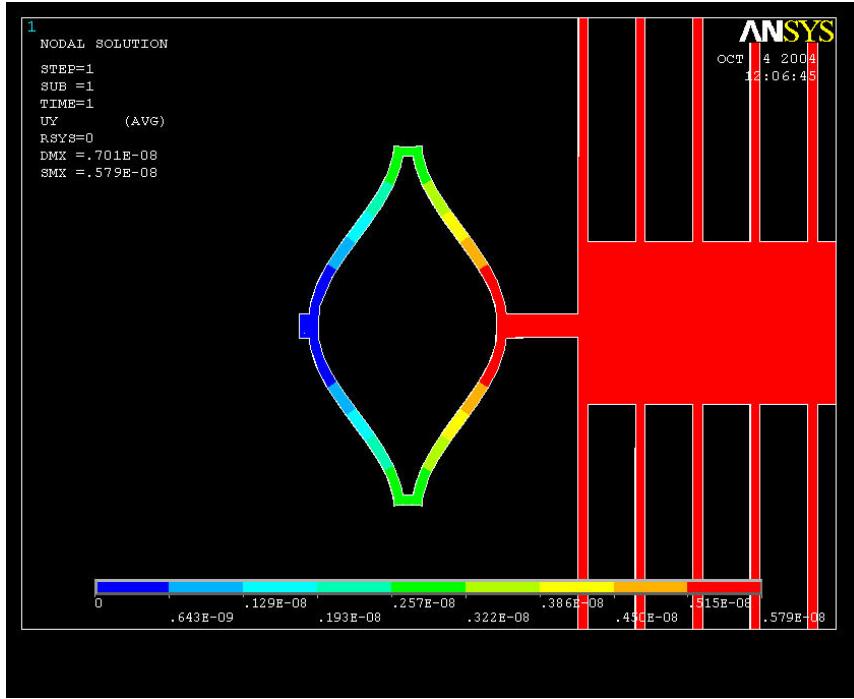

Figure 19.   Expanded y-displacement for extension side under 225g.
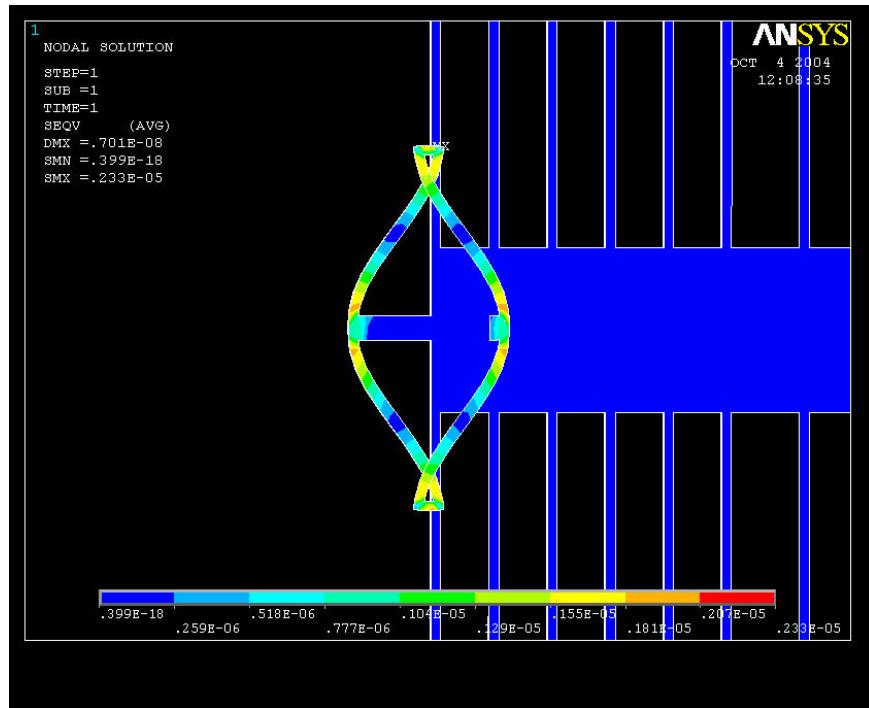
Figure 20.   Stress in y-direction for compression side under 225g
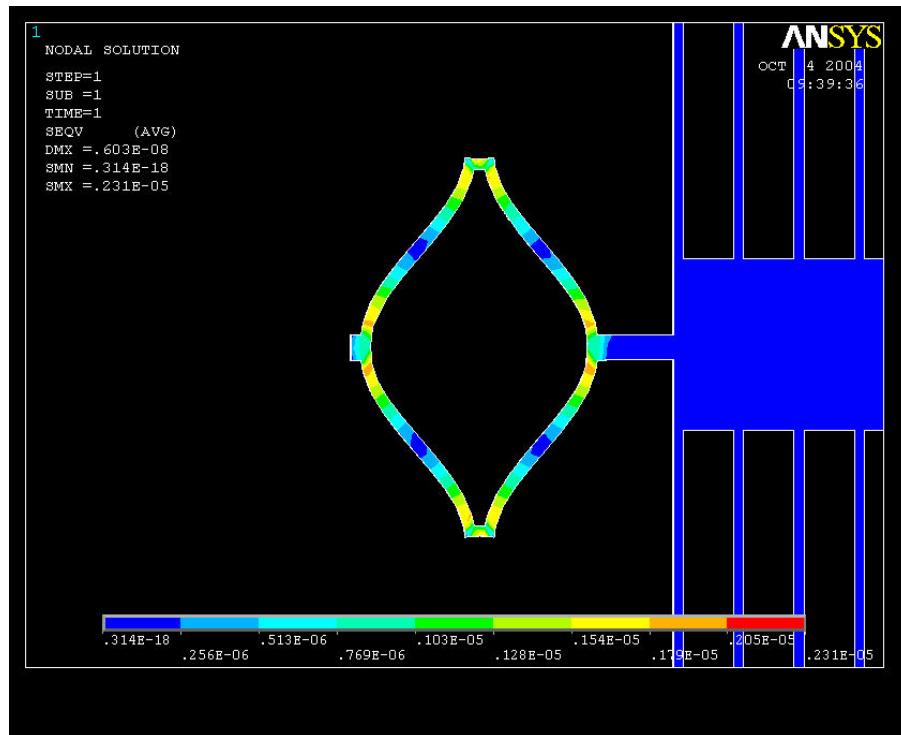
Figure 21.   Stress in y-direction for extension side under 225g

THIS PAGE INTENTIONALLY LEFT BLANK

V. FUNCTIONAL ANALYSIS

A. OUTPUT VOLTAGE AND DISPLACEMENT

The basic working principle of this accelerometer was based on the fact that under an external acceleration a proof mass was displaced a small distance which changed the gap distance between electrodes, which behaved as varying capacitors. Since the moveable electrodes were located between two fixed electrodes which were biased using two voltage supplies with equal magnitudes and opposite the device could be described by the following equivalent electrical circuit [23], where the C_1 and C_2 were variable capacitors.
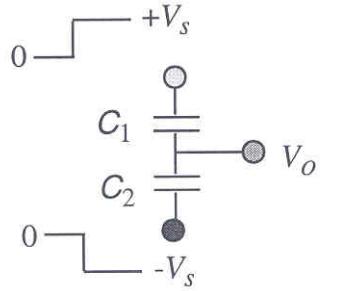
Figure 22.   Equivalent electrical circuit of the accelerometer [From: Ref. 23].

It could be easily shown that the output voltage (V_o) of the circuit in Figure 22 was given by:

$$V_{out} = -V_s + \frac{C_1}{C_1 + C_2}[V_s - (-V_{s)}]$$

$$= \frac{C_1 - C_2}{C_1 + C_2}V_s \tag{8}$$

The capacitances C_1 and C_2 were not fixed due to the motion of the electrodes attached to the proof mass. When the moveable electrodes were at rest position, the two capacitances were equal and the output voltage was zero. However, under acceleration

the movable electrodes displaced and the gaps between fixed and movable electrodes will change by amount of δx as shown in Figure 23.
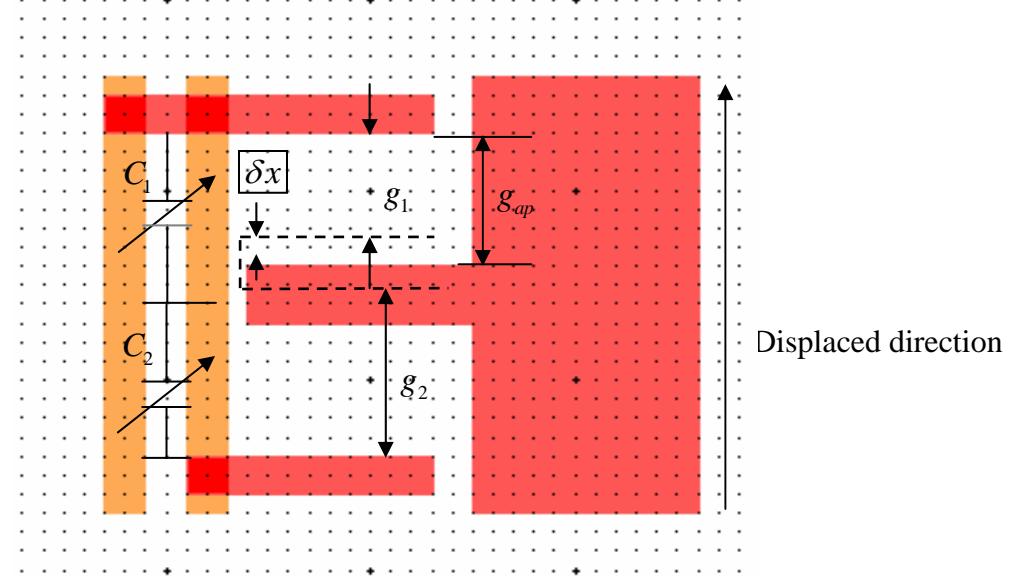
Figure 23.   Displacement of moveable electrode due to acceleration.

Thus, the output voltage as a function of displacement (δx), original gap (g_{ap}) and input voltage magnitude (V_s) weres given by:

$$g_1 = g_{ap} - \delta x$$

$$g_2 = g_{ap} + \delta x$$

$$V_{out} = \frac{C_1 - C_2}{C_1 + C_2} V_s = \frac{\dfrac{\varepsilon A}{g_1} - \dfrac{\varepsilon A}{g_2}}{\dfrac{\varepsilon A}{g_1} + \dfrac{\varepsilon A}{g_2}} V_s = \frac{\dfrac{g_2 - g_1}{g_1 g_2}}{\dfrac{g_2 + g_1}{g_1 g_2}} V_s$$

$$= \frac{\delta x}{g_{ap}} V_s \tag{9}$$

Since the displacement was related to the acceleration via

$$\delta x = \frac{a}{(\sqrt{\dfrac{k}{m}})^2} = \frac{a}{\omega_0^2}, \tag{10}$$

one could find that the output voltage and the applied acceleration has a linear relationship given in Equation (11).

$$V_{out} = \frac{\delta x}{g_{ap}} V_s = \frac{a}{g_{ap}\omega_0^2} V_s \qquad (11)$$

The V_{out} was calculated using the design parameters for a given acceleration (0 to 50g) and the results were shown in Figure 24. In addition, the output voltage was also estimated using ANSYS simulation to obtain the displacement as shown in Table 6. From the Figure 24, it can be seen that the calculated and simulated output voltages matched with 5%. The linear relationship in Figure 24 was resulted from the linear dependence of output voltage with displacement.

Table 6.   Calculated and simulated Output voltages for different accelerations (input voltage to the sensing capacitor is 15V).

Acceleration (g)	Mass (Kg)	Output Values				Voltage Difference %
		Displacement (m)		Voltage (volt)		
		Calculation	ANSYS	Calculation	ANSYS	
0		0	0	0	0	0
10		2.42×10^{-10}	2.33×10^{-10}	1.81×10^{-3}	1.75×10^{-3}	4.0%
20	2.81×10^{-10}	4.83×10^{-10}	4.67×10^{-10}	3.62×10^{-3}	3.50×10^{-3}	3.8%
30		7.25×10^{-10}	6.99×10^{-10}	5.44×10^{-3}	5.24×10^{-3}	4.0%
40		9.66×10^{-10}	9.30×10^{-10}	7.25×10^{-3}	6.98×10^{-3}	4.3%
50		1.21×10^{-9}	1.16×10^{-9}	9.09×10^{-3}	8.70×10^{-3}	4.5%
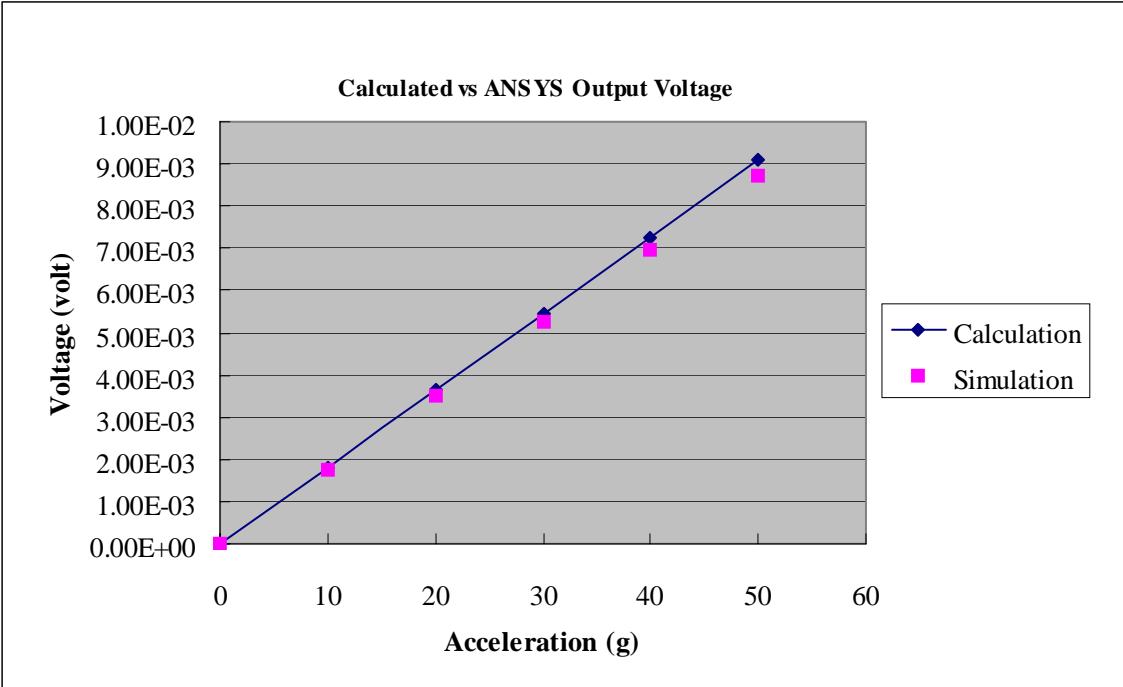
Figure 24.   Comparison of calculated and simulated output voltages.

B.   STABILITY ANALYSIS

The purpose of a stability analysis was to check whether the movable electrodes could remain within the stable equilibrium range when the various accelerations were applied. If the net force approached an unstable point, the electrodes would have the possibility to hit the fixed structures and arc and/or brake away. We could use the graph in Figure 25 to understand the stability of an accelerometer design [22]. It showed the normalized electrostatic and spring forces as a function normalized displacement. The equilibrium points correspond to when the two forces were the same as shown in Figure 26 by dark circles. For the parameters used in this example, there were two equilibrium points (P1 and P2). The stability of these points can be analyzed as follows.
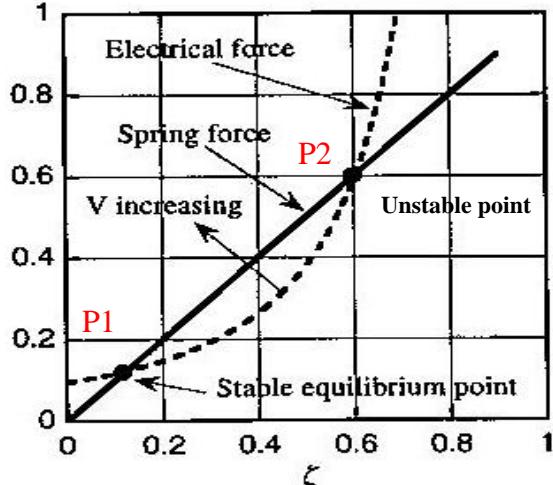
Figure 25.   Electrical and spring forces for voltage-controlled parallel-plate capacitor in normalized coordinates [From: Ref. 24].

The point P1 was stable since the any increase of the displacement will increase the repulsive spring force compared to the attractive electrostatic force that tended to reduce the displacement. Similarly for any reduction of displacement at this point will increase the attractive electrostatic force compared to the repulsive spring force, which tended to increase the displacement. Thus the point P1 was stable. The opposite was true for the point P2 making it unstable. However, as the bias voltage increased the curve for electrostatic force moves upwards as indicated in Figure 26 and the two points merged at a critical voltage known as the pull-in voltage [24]. Beyond this bias there were no equilibrium points and the accelerometer was unstable. At pull-in voltage, the displacement is equal to $g_{ap}/3$ and the magnitude of the pull-in voltage can be obtained by [24]

$$V_{pi} = \sqrt{\frac{8Kg_{ap}^2}{27\varepsilon A}} \qquad (12)$$

The Figure 26 showed the two forces as a function of displacement for our accelerometer when the bias was equal to the pull-in voltage. Using Equation (12), it was found that the pull-in voltage of our device was 390 V. Thus, the input DC voltage of 11

33

V to achieve 225g during the self-test will not push the accelerometer into the unstable region.

Pull-In Point
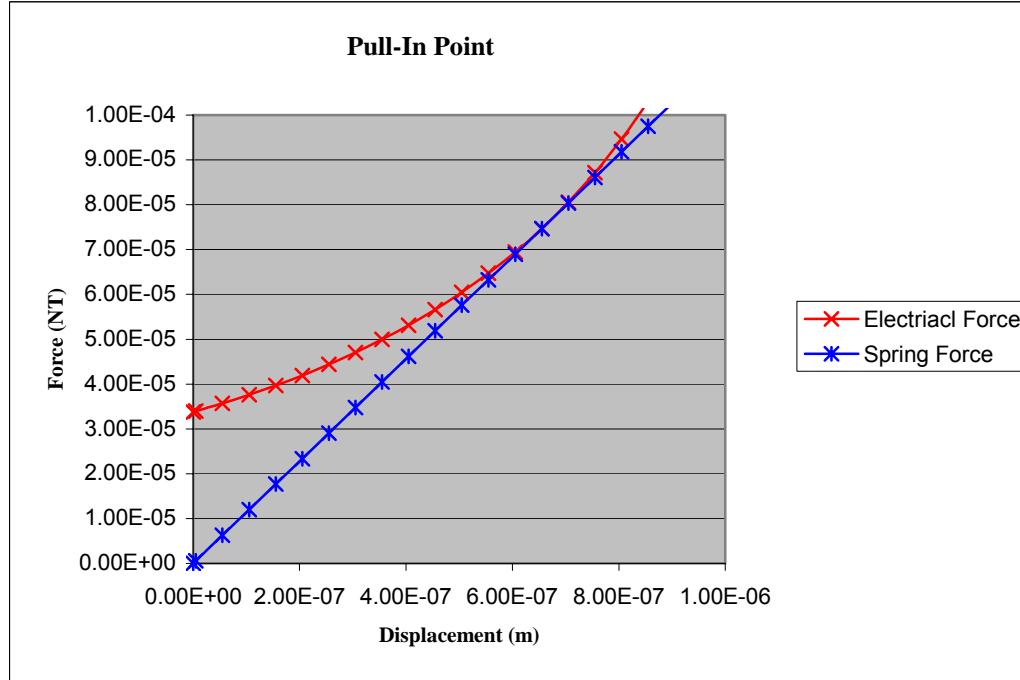
Figure 26.   Electrostatic and spring forces at pull-in voltage.

C.   ACCELERATION VS. SELF-TEST VOLTAGE

During the self-testing of the accelerometer, a DC bias was applied to the 24 self-test electrodes to exert an electrostatic force on the moving electrodes. Note that the voltage was applied to one of the fixed electrodes that sandwiched each moving electrode (see Figure 5) to avoid the cancellation of electrostatic forces if both the electrodes are biased. This force will move the proof mass along with the moving electrodes and equilibrium will reach when the spring and electrostatic forces were the same. The force generated by the DC bias can be calculated using Equation (13).

$$F = ma = \frac{\varepsilon A V^2 (24)}{2 g_{ap}^{\ 2}} \qquad (13)$$

The blue curve of Figure 27 showed the calculated acceleration as a function of DC bias. It can be seen that the 50g of acceleration can be obtained by applying about 5 V bias.
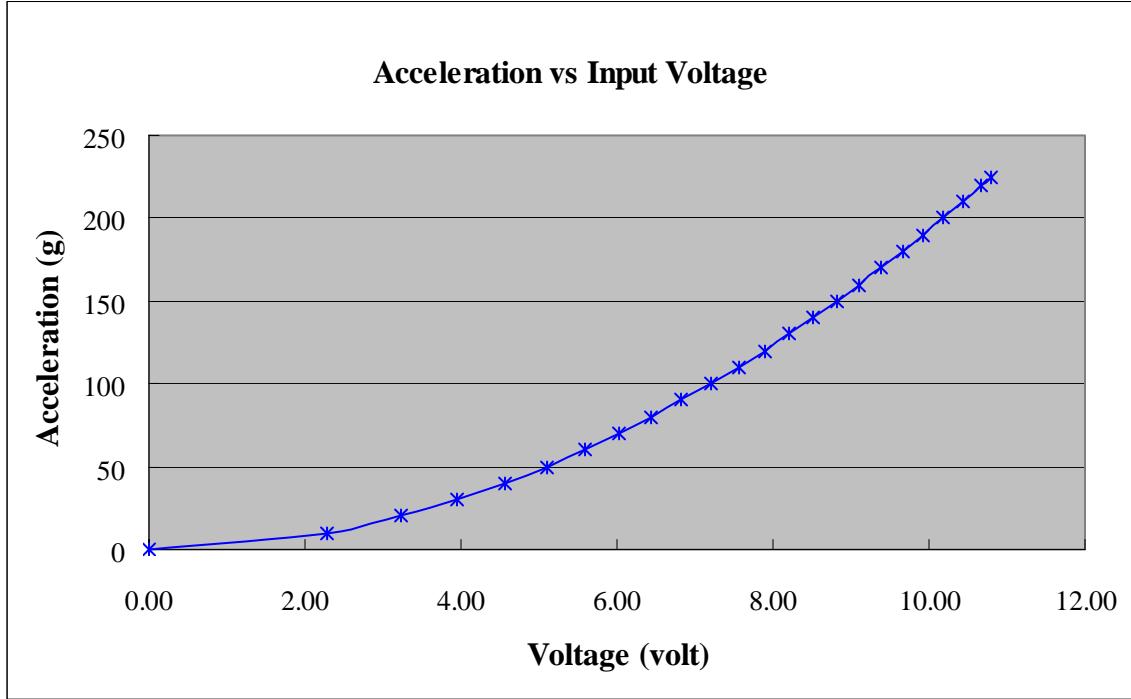
Figure 27.   Acceleration as a function of self-test voltage.

D.   SENSITIVITY

The sensitivity of the accelerometer for a given acceleration can be estimated using

$$V_{out} = \frac{a}{g_{ap}\omega_0^2}V_s.$$
(14)

Using the design parameters, the sensitivity of the accelerometer was found to be about 7 mV/g. This corresponded to an output voltage of 0.36 V at 50g acceleration. It can be seen from Equation (14) the sensitivity was strongly dependent on the resonant frequency that depended on the required bandwidth of operation.

E.   SIGNAL-TO-NOISE RATIO

There were two primary noise sources intrinsic to the accelerometer; displacement of the proof mass due to thermally driven vibrations and change in output voltage as a result of charge fluctuations on the sensing capacitor. These two effects can be analyzed using the energy stored in the spring and the sensing capacitor as follows:

$$\frac{1}{2}CV_{NC}^2 = \frac{1}{2}K_BT \tag{15}$$

$$\frac{1}{2}(2K)x^2 = \frac{1}{2}K_BT \tag{16}$$

where V_{NS} was the noise coming from mechanical vibrations and V_{NC} was the noise associated with charge fluctuations on the sensing capacitor. Using the Equation (15) and (16), the corresponding voltage fluctuations can be obtained as

$$V_{NC} = \sqrt{\frac{K_BT}{C}} \tag{17}$$

$$V_{NS} = \sqrt{\frac{K_BT}{2K}} \tag{18}$$

It can be seen that the dominant noise comes from the thermal fluctuation of charge on the capacitor. The output signal for a given acceleration can be obtained from Equation (19) and thus the signal-to-noise ratio could be estimated using

$$dB = 20\log\frac{V_{out}}{V_N} \tag{19}$$

Assuming the worse case of scenario, where a temperature of 85°C was reached and when the total capacitance of the device (100 fF) was used, V_N was about 225 μV. Figure 28 showed the calculated signal to noise ratio (SNR) as a function of acceleration assuming g_{ap} = 2 μm and V_s = 15 V. From Figure 28, it can be seen that a signal to noise ratio of 3 to 1 could be obtained when the acceleration is 1.3g.
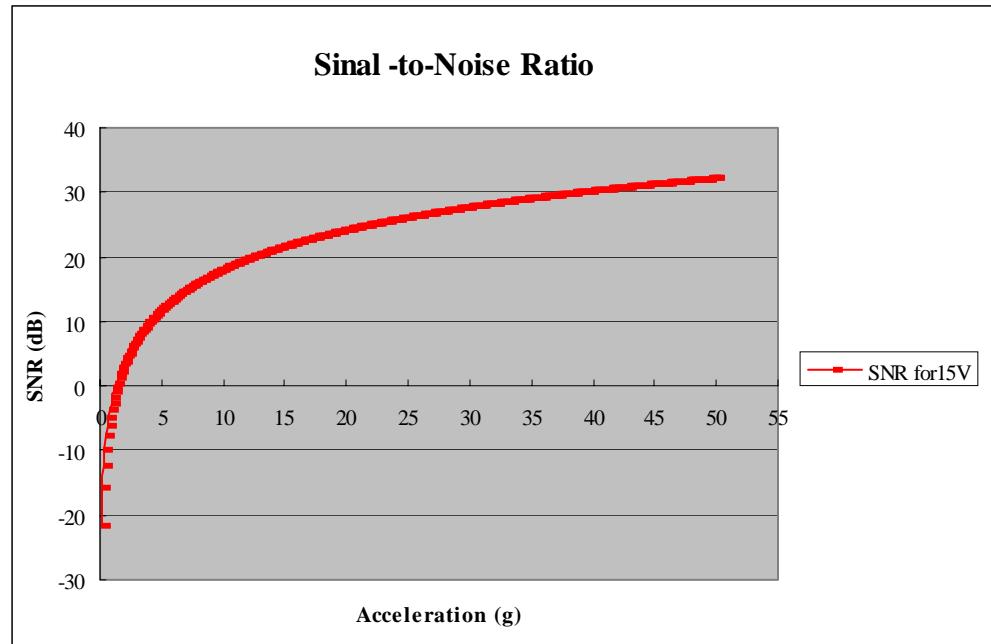
Figure 28.   SNR value for 15V in sensing region.

The above analysis showed that the designed accelerometer could be operated with good stability in the 0 to 50g ranges. It also can withstand the required 225g shocks without damaging the springs or pushing the accelerometer to unstable region. The two-axes operation can be achieved by placing identical accelerometers with displacement axes perpendicular to each other.

THIS PAGE INTENTIONALLY LEFT BLANK

VI. CONCLUSION

Two main functions were performed in this accelerometer design. First, the sensing region was designed to measure the acceleration, which produced a change in displacement of the proof mass, which changed the distance between electrodes and it produced a change in capacitance – easily measured. Second, a self-test region was designed within the accelerometer to facilitate self-tests/diagnostics of each individual accelerometer.

Finite element simulations were performed and their results indicated that when ignoring second and higher order terms result in very good agreement. The simple calculations results ranged from 2.7% to 4.3% away from the highly complex and time-consuming simulations.

The current design resulted in a very high spring force, which was strong enough to prevent the movable electrodes from hitting the fixed electrodes under the largest foreseeable accelerations (225g). This was favorable for stability, as the current design will never reach the unstable region of operations. Under the current design, a sensitivity of only $7mV/g$ was achieved.

Since PolyMUMPS provideds three layers to construct the device and since only two layers (poly0 and poly1) were used in the current design, there was one more layer available to extend the accelerometer design.

Future work was also required to extend the 2-axis accelerometer into a 3-axis design. Building the third axis on the same planar design space will require some innovation.

THIS PAGE INTENTIONALLY LEFT BLANK

LIST OF REFERENCES

[1] http://www.allaboutmems.com/whatismems.html; accessed on Aug. 15, 2004

[2] http://www.memsnet.org/mems/what-is.html; accessed on Sep. 20, 2004

[3] http://www.people.cornell.edu/pages/akt1/what.html; accessed on July 8, 2004

[4] http://www.allaboutmems.com/whatismems.html; accessed on Sep. 28, 2004

[5] http://www.ee.byu.edu/ee/iml/research/mems/mems-explained2.html; accessed on Sep. 6, 2004

[6] Stephen D. Senturia, "MICROSYSTEM DESIGN", pp. 499, 2003

[7] L. M. Roylance and J. A. Angell, "A batch-fabricatrd silicon accelerometer," IEEE Trans. Electron Devices, vol. ED-26, pp. 1911-1917, Dec. 1979

[8] Navid Yazdi, Farrokh Ayazi, Khalil Najafi," Micromachined Initial Sensors", PROCEEDINGS OF THE IEEE, VOL. 86, NO. 8, pp 1642~1646, AUGUST, 1998

[9] F. Rudolf, A. Jornod, and P. Bencze, "Silicon microaccelerometers," in Tech. Dig. 4th Int. Conf. Solid-State Sensors and Actuators (Transducers'87), Tokyo, Japan, pp. 376-379, June 1987

[10] T. W. Kenney, S. B. Waltman, J. K. Reynolds, and W. J. Kaiser, "A micrimachined silicon electron tunneling sensor," in Proc. IEEE Micro Electro Mechanical Systems Workshop (MEMS'90), Napa Valley, CA, pp. 192-196, 1990

[11] H. K. Rocksatd, T. W. Kenney, J. K. Reynolds, W. J. Kaiser, and T. B. Gabrielson, "A miniature high-sensitivity broad-band accelerometer based on electron tunneling transducers," Sensors Actuators A, vol. 43, pp. 107-114, 1994

[12] R. Hiratsuka, D. C. van Duyn, T. Otraedian, and P. de Vries, "A novel accelerometer based on a silicon thermopile," in Tech. Dig. 6th Int. Conf. Solid-

State Sensors and Actuators (Transducers'91), san Francisco, CA, pp. 420-423, June 1991

[13] M. Leung, J. Jones, E. Czyzewska, J. Chen, and B. Woods, "Micromachined accelerometer based on convection heat transfer, " In Proc. IEEE Micro Electro Mechanical Systems Workshop (MEMS'98), Heidelberg, Germany, pp. 627-630, Jan. 199

[14] Xinping Cao, Dacheng Zhang, Ru Huang, Xing Zhang, "The design and fabrication of a miniaturized differential-capacitive triaxial accelerometer", Peking University, pp 1, 2001

[15] C. Yeh and K. Najafi, "A low-voltage bulk-silicon tunneling-based microaccelerometer," in Tech. Dig. IEEE Int. Electron Devices Meeting (IEDM), Washington, DC, pp. 593-596, Dec. 1995

[16] L. M. Roylance and J. A. Angell, "A batch-fabricatrd silicon accelerometer," IEEE Trans. Electron Devices, vol. ED-26, pp. 1911-1917, Dec. 1979.

[17] http://www.memsrus.com/mumps.pdf; accessed on Nov. 2, 2004

[18] ANSYS 7.1 documentation, Copy Right 2003 SAS IP, Inc

[19]. http://www.memscap.com/memsrus/svcssched.html; accessed on Nov. 15, 2004

[20] Stephen D. Senturia, "MICROSYSTEM DESIGN", pp. 518, 2003

[21] Stephen D. Senturia, "MICROSYSTEM DESIGN", pp. 519, 2003

[22]http://www.ee.ucla.edu/~wu/ee250b/case_study_1_accelerometer.pdf; accessed on Nov. 20, 2004

[23] Stephen D. Senturia, "MICROSYSTEM DESIGN", pp. 502, 2003

[24] Stephen D. Senturia, "MICROSYSTEM DESIGN", pp. 136, 2003

INITIAL DISTRIBUTION LIST

1. Defense Technical Information Center
   Ft. Belvoir, Virginia

2. Dudley Knox Library
   Naval Postgraduate School
   Monterey, California

3. Professor Karunasiri, Gamani
   Department of Physics
   Naval Postgraduate School
   Monterey, California

4. Professor Sinibaldi, Jose
   Department of Mechanical and Astronautical Engineering
   Naval Postgraduate School
   Monterey, California